ADVANCED MATERIALS
www.advmat.de

# Selenic Acid Etching Assisted Vacancy Engineering for Designing Highly Active Electrocatalysts toward the Oxygen Evolution Reaction

*Lin Zhang, Chengjie Lu, Fei Ye, Ruilvjing Pang, Yang Liu, Zeyi Wu, Zongping Shao,* Zhengming Sun, and Linfeng Hu**

**Oxygen evolution electrocatalysts are central to overall water splitting, and they should meet the requirements of low cost, high activity, high conductivity, and stable performance. Herein, a general, selenic-acid-assisted etching strategy is designed from a metal–organic framework as a precursor to realize carbon-coated 3d metal selenides $M_mSe_n$ ($Co_{0.85}Se_{1-x}$, $NiSe_{2-x}$, $FeSe_{2-x}$) with rich Se vacancies as high-performance precious metal-free oxygen evolution reaction (OER) electrocatalysts. Specifically, the as-prepared $Co_{0.85}Se_{1-x}$@C nanocages deliver an overpotential of only 231 mV at a current density of 10 mA cm$^{-2}$ for the OER and the corresponding full water-splitting electrolyzer requires only a cell voltage of 1.49 V at 10 mA cm$^{-2}$ in alkaline media. Density functional theory calculation reveals the important role of abundant Se vacancies for improving the catalytic activity through improving the conductivity and reducing reaction barriers for the formation of intermediates. Although phase change after long-term operation is observed with the formation of metal hydroxides, catalytic activity is not obviously affected, which strengthens the important role of the carbon network in the operating stability. This study provides a new opportunity to realize high-performance OER electrocatalysts by a general strategy on selenic acid etching assisted vacancy engineering.**

L. Zhang, Z. Y. Wu, Prof. L. F. Hu
Department of Materials Science
Fudan University
Shanghai 200433, P. R. China

Dr. C. J. Lu, Dr. F. Ye, R. L. J. Pang, Y. Liu, Prof. Z. M. Sun, Prof. L. F. Hu
School of Materials Science and Engineering
Southeast University
Nanjing 211189, P. R. China
E-mail: linfenghu@seu.edu.cn

Prof. Z. P. Shao
WA School of Mines: Minerals, Energy and Chemical Engineering (WASM-MECE)
Curtin University
Perth, Western Australia 6102, Australia

Prof. Z. P. Shao
State Key Laboratory of Materials-Oriented Chemical Engineering
College of Chemical Engineering
Nanjing Tech University (NanjingTech)
Nanjing 210009, P. R. China
E-mail: shaozp@njtech.edu.cn

The ORCID identification number(s) for the author(s) of this article can be found under https://doi.org/10.1002/adma.202007523.

**DOI: 10.1002/adma.202007523**

The development of environment-friendly and sustainable conversion technologies is of great significance in storing and utilizing renewable energy.[1–3] For example, hydrogen production via electrochemical water splitting is considered as one of the most promising methods for the facile storage and high-quality utilization of renewable energy.[4–6] However, its practical use is strongly dependent on the cost and efficiency. Water splitting involves two half reactions, that is, the oxygen evolution reaction (OER) at the anode and hydrogen evolution reaction at the cathode, which determines the efficiency of water splitting. Actually, OER also plays a crucial role in many other modern electrochemical energy conversion and storage processes such as rechargeable metal–air batteries and regenerative fuel cells.[7–9] Slow OER kinetics has been a main concern for the widespread use of electrochemical water splitting for hydrogen production, which is closely related to the complex proton-coupled multiple charge transfer process, resulting in high overpotential for triggering the reaction.[10,11] During the past, precious metal $RuO_2$-based oxides were widely used as the electrocatalysts to promote OER, which, however, suffers from high cost and insufficient stability.

Nowadays, more and more efforts have been conducted toward the development of cost-effective OER electrocatalysts with improved activity and durability. Since the activity of a catalyst is directly related to both the number of active sites and the intrinsic activity, the strategies to increase both these two parameters have been intensively exploited. Considering the high price of noble metals, nonprecious metal oxides, sulfides, and selenides have attracted considerable attention as alternative OER electrocatalysts. Metal–organic frameworks (MOFs) are a category of amazing crystalline materials with ultrahigh porosity (up to 90% free volume) and enormous internal surface areas, extending beyond 6000 m$^2$ g$^{-1}$,[12,13] which can also be served as an excellent material platform to form transition metal derivatives with well-defined hollow morphology.[14,15] Recently, hollow-structured nanocages of transition metal selenides derived from MOFs were suggested to be promising electrocatalysts because of their large exposed surface areas,

 

abundant active sites, and the intrinsic high conductivity of transition metal selenides.[16–18]

On the other hand, vacancy engineering has been proposed as an effective strategy for tuning the intrinsic OER activity of metal oxides, metal sulfide, and metal selenides.[19–21] It was demonstrated that the surface vacancies can greatly influence the electronic structure of electroctalysts, while a structure with proper vacancies is essential to achieve ideal intermediate binding energies which holds the key for the construction of highly efficient OER electrocatalysts.[22,23] If one can incorporate a proper amount of structural vacancies into the transition metal selenide, improved catalytic activity may be realized. However, up to date, most MOF derivatives of transition metal selenide were produced by the direct high-temperature calcination of MOFs precursor and Se powder at 400–600 °C, while such a high-temperature process generally led to high-crystalline products with rather poor surface vacancies.[24,25] Therefore, how to design the MOF derivatives with abundant vacancies is in great request and remains a big challenge. In addition, it was reported, under OER condition, metal selenides, metal sulfide, and metal phosphates could be transferred to metal oxides or metal hydroxides, which usually show much poor electrical conductivity than the precursors. Thus, the durability is also a big concern for such electrocatalysts.

Herein, we report a general selenic-acid-assisted etching strategy to synthesize 3d metal selenides $M_mSe_n$ ($Co_{0.85}Se_{1-x}$, $NiSe_{2-x}$, $FeSe_{2-x}$) with rich Se vacancies as OER electrocatalysts with outstanding activity and favorable durability. The selenic acid partially etches ZIF-67 framework and also acts as a source of selenium under a mediate condition, finally carbon layer-coated $M_mSe_n$ derivatives were obtained after a subsequent calcination at intermediate temperature under inert atmosphere, as schematically illustrated in **Scheme 1**. Most importantly, compared with the conventional one-step calcination method,[24,25] the current selenic-acid-assisted etching strategy successfully introduced rich Se vacancies into the $M_mSe_n$/C hollow structures, which gives rise to a great increase in the number of active sites, enhancement of the electronic conductivity, and thereby decreased energy barrier for the formation of intermediates, consequently significantly improved catalytic activity for OER in a strong alkaline medium was observed. Although, as expected, the cobalt selenides were slowly transformed into cobalt hydroxides under continuous OER operation, the activity was not largely affected due to the high activity of in situ formed cobalt hydroxides, the reserve of porous structure for efficient mass transfer, and the high conductivity as provided by the carbon component. Our study provides a new opportunity to realize high-performance OER electrocatalysts by a general strategy on selenic acid etching assisted vacancy engineering.

Our work started with the mechanical stirring of $SeO_2$ powder and uniform polyhedron ZIF-67 nanocrystals in methanol aqueous solution. Known that the dissolution of $SeO_2$ in water forms selenous acid,[26,27] we found that such a weak acid solution gradually etched ZIF-67 framework to produce $Co^{2+}$. Compared with pristine ZIF-67 which demonstrates a regular, rhombic dodecahedron morphology, and smooth surface (Figure S1a–c, Supporting Information), the products after etching for 1 h (noted as ZIF-1h, Table S1, Supporting Information) well retained the dodecahedral morphology

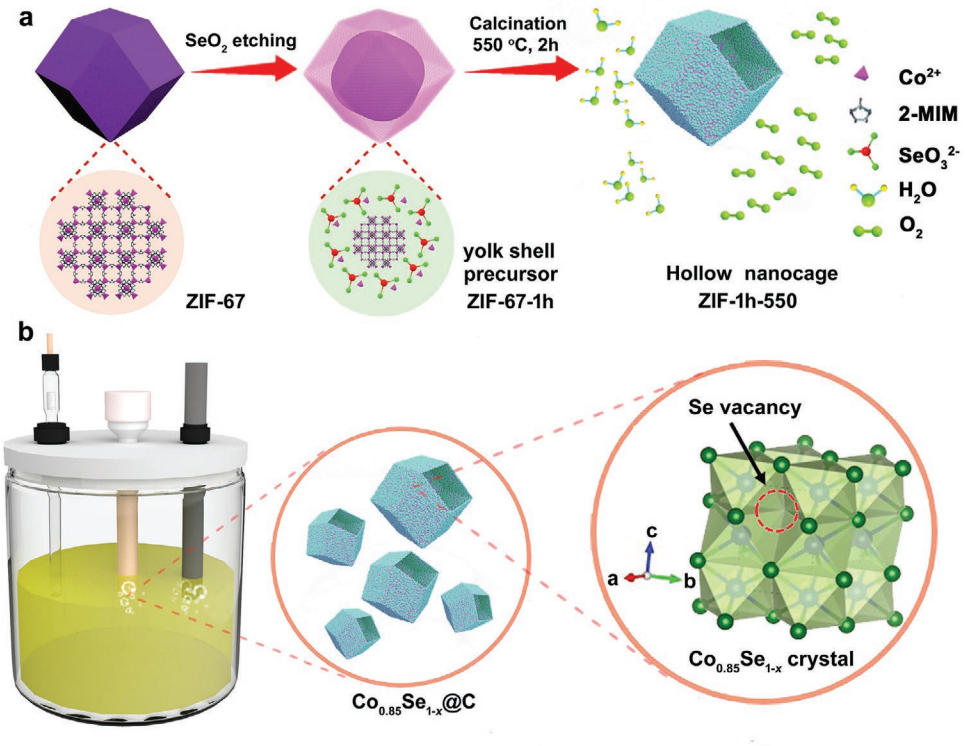


**Scheme 1.** Schematic illustration of the routes to $Co_{0.85}Se_{1-x}$@C hollow nanocages with rich Se vacancy and its OER electrode application.

 

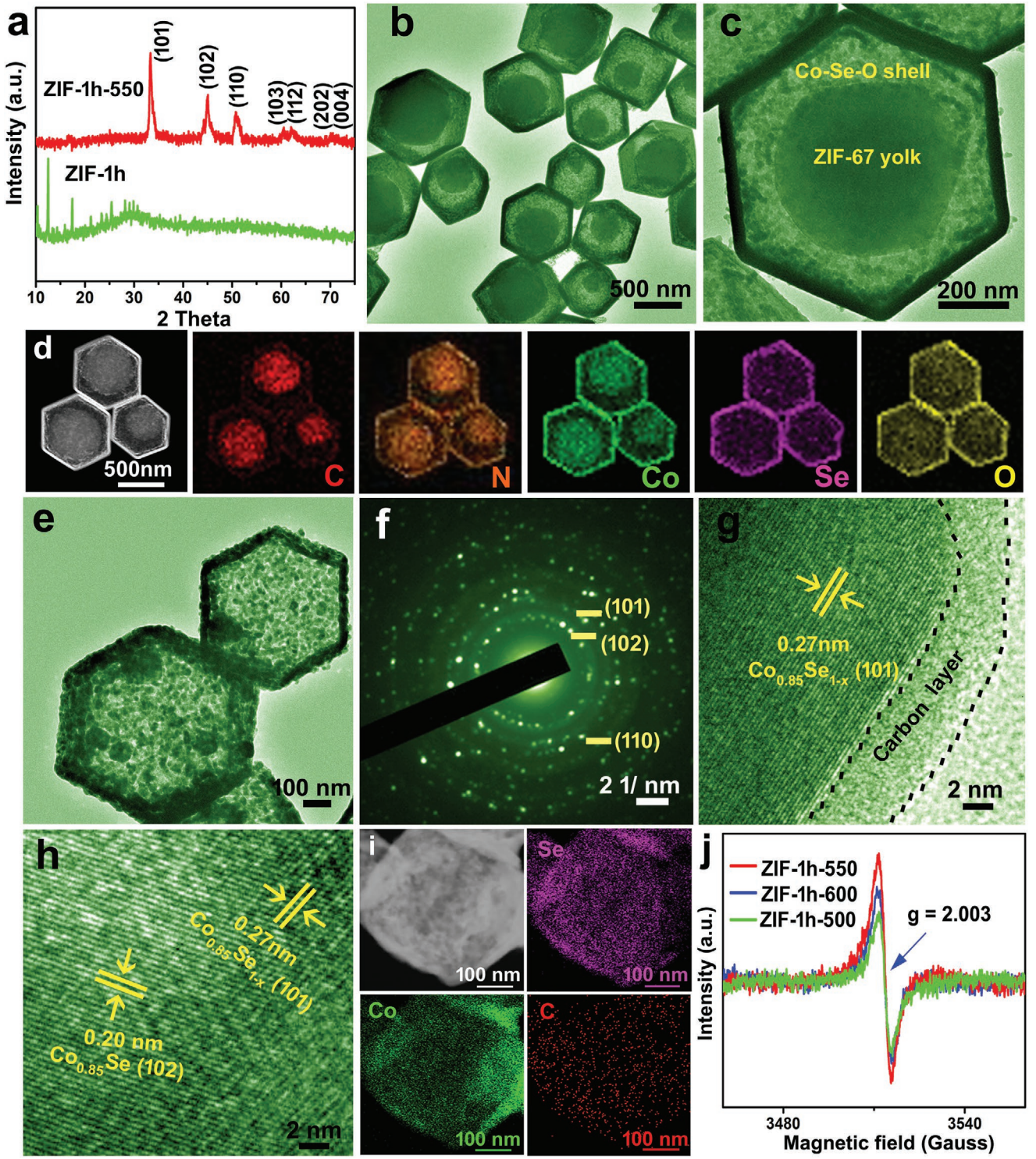


**Figure 1.** a) Typical XRD patterns of ZIF-1h, and ZIF-1h-550 ($Co_{0.85}Se_{0.51}\square_{0.49}$@C). b,c) TEM images and d) EDS Elemental mapping of C, N, Co, Se, O elements of ZIF-1h. e–h) TEM, HRTEM, and corresponding SAED pattern of ZIF-1h-550. i) EDS elemental mapping of C, Co, Se elements in ZIF-1h-550. j) EPR spectra of ZIF-1h-500, ZIF-1h-550, and ZIF-1h-600 samples, respectively.

accompanied with a rougher surface (Figure S1d, Supporting Information). X-ray diffraction (XRD) pattern (**Figure 1**a) of the ZIF-1h sample shows the similar peaks as that of pristine ZIF-67 but with a much lower diffraction intensity. Further observation in the transmission electron microscopy (TEM) image indicates the formation of abundant yolk–shell nanocages with size of 500–600 nm (Figure 1c,d). The representative energy-dispersive X-ray spectroscopy (EDS) elemental mapping

analysis confirmed the compositional elements of the inner yolk are only C, N, and Co, meanwhile Co, Se, O elements are homogeneously distributed in the outer shell of the nanocages. High-resolution transmission electron microscopy (HRTEM) image and the corresponding selected area electron diffraction (SAED) pattern confirm the absence of any lattice fringe in the shell layer (Figure 1e,f), demonstrating its amorphous nature. All the results reveal the as-etched nanocages with a characteristic structure of ZIF-67 yolk@Co–Se–O amorphous shell. Accordingly, the etching process preferentially started from the edge of ZIF-67 polyhedrons due to its more structural defects, and followed by the surface-energy-driven crystallization process.[28] However, ZIF-67 could not be completely etched even though prolonging the etching time up to 10 h. It should be noteworthy that ZIF-67 was drastically etched to form hollow structure in the case of phytic acid and hydrochloric acid reported previously.[29,14] The formation of a yolk–shell structure in our designed system should be ascribed to the weak acidity of selenic acid. We found that room-temperature aging at ≈1 h is favorable to the well-defined yolk–shell morphology (Figures S2,S3, Supporting Information), while longer aging of 2–10 h and any hydrothermal treatment at elevated temperatures generally gave rise to the drastic damage of initial ZIF-67 polyhedron and irregular shape of the sample (Figures S4,S5, Supporting Information).

We subsequently annealed this yolk-shell precursor at 550 °C under Ar flow (noted as ZIF-1h-550). The formation of $Co_{0.85}Se$-typed phase (JCPDS no. 52-1008) after annealing is confirmed by the powder XRD pattern (Figure 1a). Scanning electron microscopy (SEM) and TEM images on an individual $Co_{0.85}Se$ demonstrated a hollow nanocage morphology (500 nm in edge length; ≈50 nm in thickness). The corresponding SAED pattern presents a typical ring of polycrystalline structure, suggesting that the wall of the as-prepared nanocages consists of numerous small nanocrystallines.[30] HRTEM characterization on an individual nanocrystal clearly displays the lattice fringes with an interplanar distance of 0.20 and 0.27 nm, corresponding to (101) and (102) planes of hexagonal $Co_{0.85}Se$ lattice, respectively (Figure 1g,h). In addition, the outer wall of our $Co_{0.85}Se$ nanocages is coated by a uniform amorphous carbon layer (thickness of 6 nm), which is similar with $MoC_x$ nano-octahedrons reported by Lou et al.[31] EDS element mapping results further confirm the presence of this carbon layer and also the uniform distribution of Co, Se atoms in the nanocages (Figure 1i). The carbon content in the resultant nanocages was determined to be ≈21.2 wt% from the thermogravimetric analysis (TG) curve (Figure S6, Supporting Information). Such carbon will provide high conductivity for facilitating the charge transfer and also an important matrix for maintaining the hollow structure during electrochemical operation, which will be discussed in more detail later. The as-prepared nanocages showed a highly mesoporous structure, as evident by a high specific Brunauer–Emmett–Teller surface area of 46.3 $m^2 g^{-1}$ and abundant micropore/mesopores mainly distributed in the range of 1.2–10 nm (Figures S7,S8, Supporting Information). The high uniformity of the pores origins from the ordered porous architecture of the ZIF-76 matrix.[32] Electron paramagnetic resonance (EPR) spectra verifies the presence of abundant selenium vacancies in the as-annealed samples. As shown in Figure 1j, the strong EPR signal at $g = 2.003$ was caused by the trapped electrons from the Se vacancies,[33] and annealing at 550 °C produced the highest Se vacancy concentration compared with that of the samples annealed at 500 and 600 °C (ZIF-1h-500 and ZIF-1h-600). Although the real origin of these Se vacancies is still not clear, we speculate the composition feature of our yolk–shell precursor may be responsible. During the pyrolysis process of the ZIF-67 yolk@Co–Se–O amorphous shell, ZIF-67 yolk collapsed at high temperature accompanied with the evaporation of C, H components in the ZIF-67 framework. Meanwhile, the Co atoms in the ZIF-67 yolk likely migrated to the Co–Se–O amorphous shell spontaneously. It is noteworthy that initial ratio of Co, Se atoms in the amorphous shell is almost 1:1 as evident by the identical intensity in the Co, Se elemental mapping as shown in Figure 1d. Therefore, the combination of Co atoms from the ZIF-67 yolk may result in the deviation in stoichiometric ratio of Co and Se and the production of rich Se vacancies in our $Co_{0.85}Se_{1-x}$@C nanocages. In addition, inductively coupled plasma (ICP) atomic emission spectroscopy verifies a Co/Se molar ratio of 1.66 for the optimal ZIF-1h-550 sample, corresponding to a chemical composition of $Co_{0.85}Se_{0.51}\square_{0.49}$@C ($x = 0.49$) with very high Se vacancy concentration.

The activity of the as-prepared samples as OER electrocatalysts was first tested by a standard three electrode system in the 1 M KOH electrolyte by using commercially $RuO_2$ as reference. The polarization curves with *iR* compensation were recorded by linear sweep voltammetry (LSV). As shown in **Figure 2**a, the ZIF-1h-550 showed a small overpotential of only 231 mV for reaching a polarization current of 10 mA $cm^{-2}$, which is significantly lower than that of ZIF-1h (282 mV) and commercial $RuO_2$ (323 mV). Figure 2b and Figures S4,S5, Supporting Information, further summarize the Tafel slope of the as-synthesized $Co_{0.85}Se_{0.51}\square_{0.49}$@C nanocages. As seen, ZIF-1h-550 demonstrated a Tafel slope of 57 mV $dec^{-1}$, which is lower than that of ZIF-67-550 (105 mV $dec^{-1}$), ZIF-67 (110 mV $dec^{-1}$), ZIF-1h (99 mV $dec^{-1}$), and $RuO_2$ (116 mV $dec^{-1}$), indicating its much faster OER reaction kinetics. Consistently, the corresponding Nyquist plots of ZIF-1h-550 also showed the smallest arc radius. The outstanding OER performance of ZIF-1h-550 is identified by its prominent double layer capacitance (325 mF $cm^{-2}$), as a comparison of only 21 mF $cm^{-2}$ for commercial $RuO_2$ (Figure S10, Supporting Information). The increased electrochemical active surface area might mainly be benefited from their hollow structures, which leads to better effective accessibility of active sites, thus bringing superior catalytic performance.[34]

In addition to catalytic activity, durability is another big concern in the development of electrocatalysts. For stability evaluation, the working electrode was handled for 5000 cycles using a continuous cyclic voltammetry measurement with the results shown in Figure 2e. There are no obvious changes of ZIF-1h-550 sample after performing 5000 CV scans of OER (8 mV decay), and the long-term chronoamperometry test at 20 mA $cm^{-2}$ demonstrated only a small negative current decay (8.5%) over 50 h, further confirming the excellent operational stability of the ZIF-1h-550 catalyst (Figure 2f). The corresponding SEM image and EDX mapping demonstrated that the morphology of the $Co_{0.85}Se_{0.51}\square_{0.49}$@C nanocage after the long-term durability test remained almost unchanged. However, Se content decreased

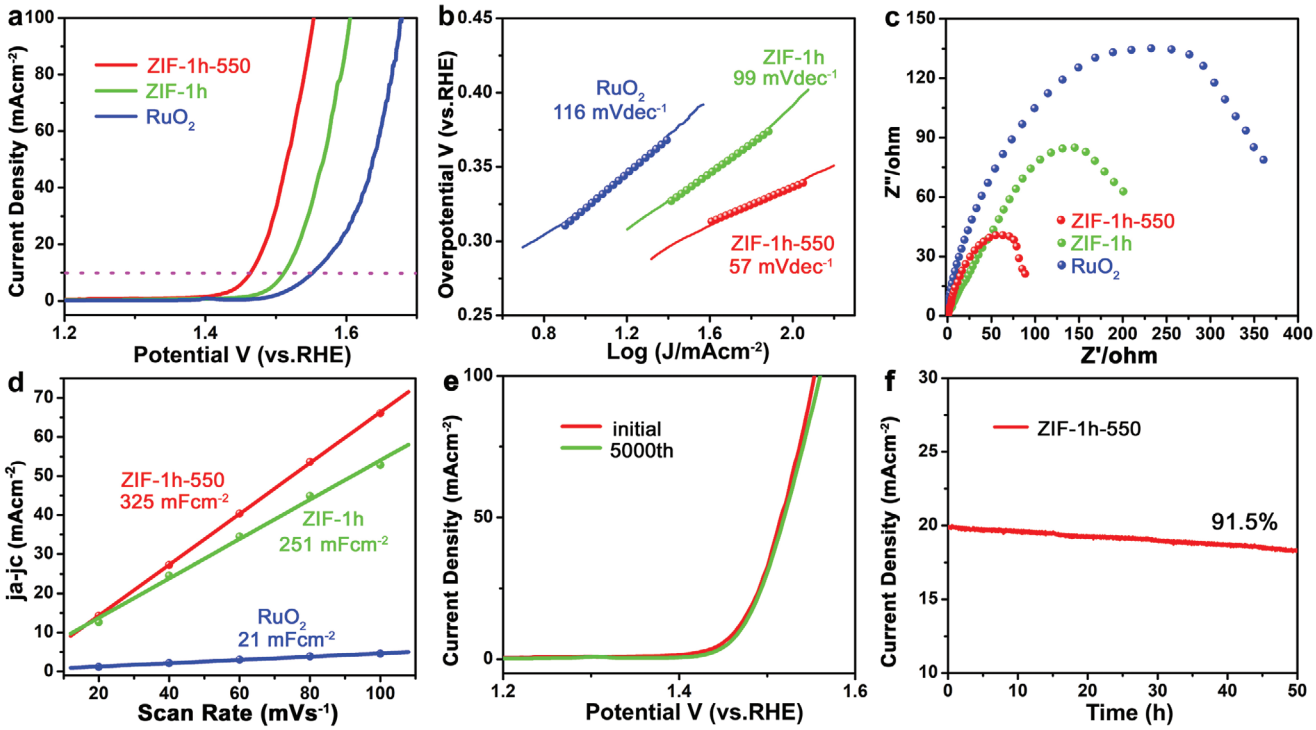


**Figure 2.** a–c) LSV curves, Tafel plots, and EIS curves for ZIF-1h-550 ($Co_{0.85}Se_{0.51}\square_{0.49}$@C), ZIF-1h, and $RuO_2$. d) Linear plots of cathodic charging currents versus the scan rate derived from cyclic voltammetry diagrams under different scan rates. e) Polarization curves for ZIF-1h-550 before and after 5000 cycles. f) *I–t* curve for ZIF-1h-550 at the $\eta_{20}$ for 50 h.

from 32% to 2% with an increase of the oxygen content from 10% to 38% during the test (Figures S11,S12, Supporting Information), implying a possible phase transformation into CoOOH during the OER process. The formation of the CoOOH phase after OER was further identified by high-resolution X-ray photoelectron spectroscopy (XPS) and PXRD characterizations during the long-term durability (Figure S13a–c, Supporting Information). Clearly, the Co—Se peak in Co $2p_{3/2}$ fades away with the appearance of the a clear Co—O peak at 781.4 eV, revealing the formation of CoOOH during the OER.[35,36] In addition, from the Se 3d spectrum in Figure S13b, Supporting Information, the convolutional area of Se 3d peak gradually decreases after OER reaction, and it completely disappears even after 5000 CVs, demonstrating the dissolution of $Co_{0.85}Se_{0.51}\square_{0.49}$ phase after the long-time CV process. This is consistent with the ICP test result (Table S2, Supporting Information) that the Se content drastically drops from 8.6% to 1.81% (atom ratio) after 5000 CVs. O 1s spectrum in Figure S13c, Supporting Information, also confirms the convolutional area of —OH group peak significantly increases during the OER process. From the PXRD patterns of the $Co_{0.85}Se_{0.51}\square_{0.49}$@C electrode before and after OER process (Figure S13d, Supporting Information), one can see the diffraction intensity of $Co_{0.85}Se_{0.51}\square_{0.49}$ phase remarkably decreased during the OER, and finally converted into almost amorphous structure after 5000 cycles. According to the above analysis, the $Co_{0.85}Se_{0.51}\square_{0.49}$ phase was gradually transformed into CoOOH as the active species during the OER process. A similar phenomenon was observed for NiSe electrocatalyst, as reported by Hu et al.[37] It is known that CoOOH is also a highly active OER electrocatalyst,[29,32] which is a semiconductor with poor conductivity. However, the large amount of the carbon (21.2 wt%) in the ZIF-1h-550 sample formed a 3D conducting network then provided sufficient conductivity even after the full transformation of $Co_{0.85}Se$ into CoOOH. In addition, such 3D carbon network provided a firm skeleton for maintaining the morphology of the catalyst as evident by the ex-situ TEM observation (Figure S14, Supporting Information). As a result, the hollow nanocage structure of the catalyst was successfully reserved after the phase transformation, ensuring efficient mass transfer and large number of active sites. Consequently, high and comparable catalytic activity was still maintained after a prolonged operation period. We also optimized the synthetic conditions on etching methods, etching time, and annealing temperature to further enhance the OER activity. The results suggested that the $Co_{0.85}Se_{0.51}\square_{0.49}$@C nanocage obtained by etching at room temperature for 1 h and then calcining in Ar at 550 °C gives the best performance (Figures S15–S20, Supporting Information).

To better understand the origin of the robust OER performance, we carried out the electrochemical comparison between our $Co_{0.85}Se_{0.51}\square_{0.49}$@C nanocage and conventional $Co_{0.85}Se$@C prepared by the one-step calcination of ZIF-67 and Se powder.[38] No obvious difference has been observed between $Co_{0.85}Se_{0.51}\square_{0.49}$@C nanocages and the $Co_{0.85}Se$@C counterpart from the powder XRD data (**Figure 3**a). Interestingly, our $Co_{0.85}Se_{0.51}\square_{0.49}$@C nanocage exhibited much lower overpotentials of 231 mV at 10 mA $cm^{-2}$, a higher turnover frequency (TOF) (1.46 $s^{-1}$) than that of $Co_{0.85}Se$ ($\eta_{10}$ = 291 mV, TOFs = 0.89 $s^{-1}$ at an overpotential of 300 mV), and much better stability (Figures S21,S22, Supporting Information). As mentioned earlier, very high Se vacancy concentration has

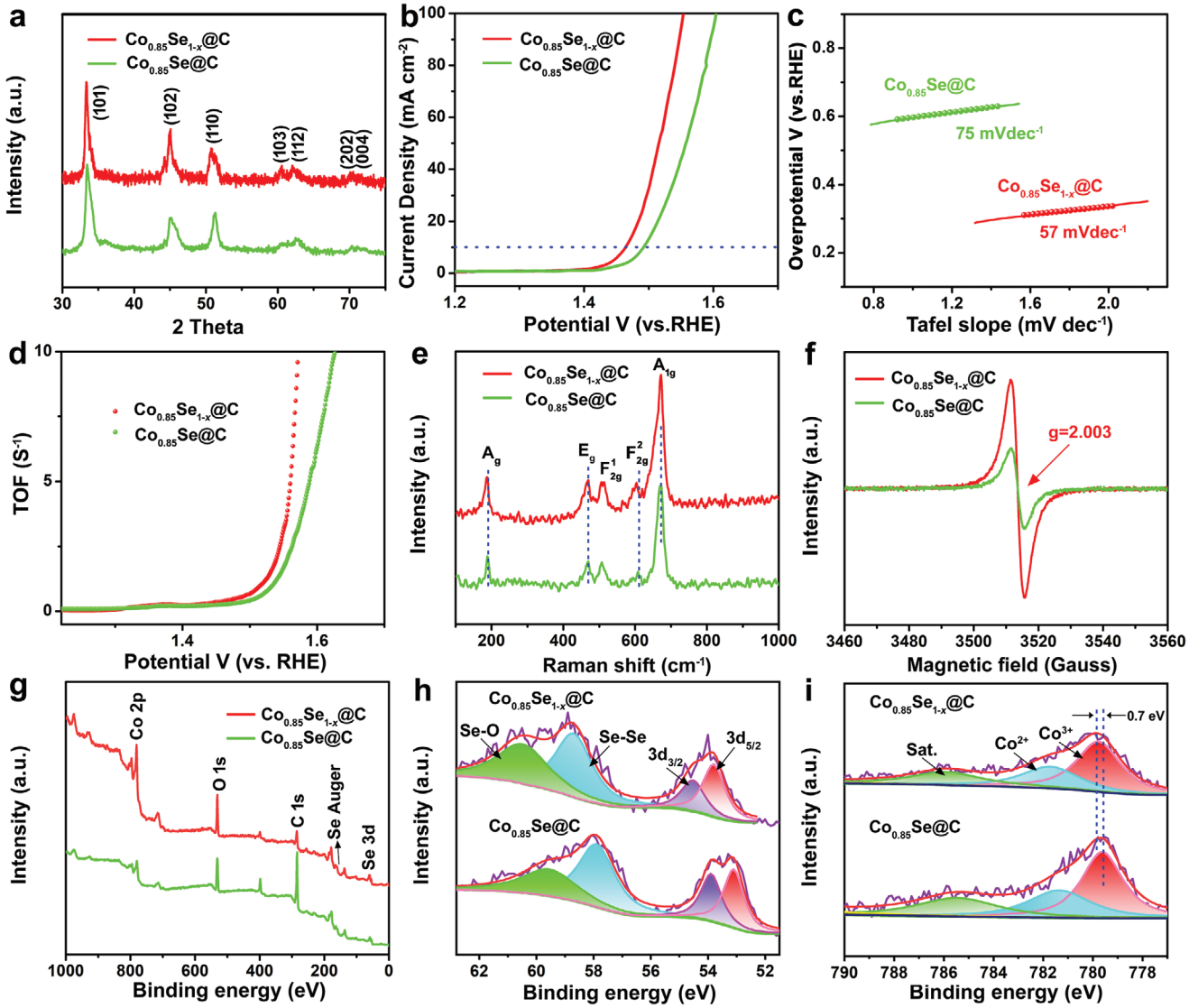


**Figure 3.** a–c) XRD pattern, LSV curves, and Tafel plots of ZIF-1h-550 and $Co_{0.85}Se$@C samples, respectively. d–f) TOF, Raman, and EPR spectra of ZIF-1h-550 and $Co_{0.85}Se$@C samples, respectively. g) Wide scan and h,i) high-resolution Se 3d and Co $2p_{3/2}$ XPS spectrum of ZIF-1h-550 and $Co_{0.85}Se$@C samples, respectively.

been detected in our $Co_{0.85}Se_{0.51}\square_{0.49}$@C nanocages (Figure 1j). Then, EPR, Raman, and XPS characterizations were further performed to systematically compare the structural discrepancy. Typically, EPR spectra (Figure 3f) delivered a much stronger resonance single at $g = 2.003$ compared with that of the $Co_{0.85}Se$@C counterparts, demonstrating a much higher concentration of Se vacancies in our sample.[33] In addition, the Raman vibrational frequencies for the Co—Se bond ($A_g$ modes) of our $Co_{0.85}Se_{0.51}\square_{0.49}$@C nanocage demonstrated red-shifted from 188.8 to 187.2 $cm^{-1}$, respectively.[39] This red-shift should be ascribed to the weakening of the Co—Se modes resulting from the escape of the Se atoms, which is consistent with results of the Se vacancy riched $ReSe_{2-x}$ as reported previously.[40,41] The difference on Se vacancy concentrations was further confirmed by the survey XPS spectra (Figure 3g–i). One can see the peak convolutional ratio of Se $3d_{3/2}$ in $Co_{0.85}Se$@C counterpart is much higher than that of the $Co_{0.85}Se_{0.51}\square_{0.49}$@C nanocage, which should be ascribed to increased number of low-coordination Se atoms with the presence of rich selenium vacancies.[42] Meanwhile, the Co 2p spectrum of $Co_{0.85}Se_{0.51}\square_{0.49}$@C sample exhibited an appreciable shift to lower energies compared with $Co_{0.85}Se$@C, further confirming a reduction of Co valence due to the formation of Se vacancies in the lattice.[43] All results reveal that our design of the selenic-acid-assisted etching strategy brought about very high concentration of Se vacancy in the products compared with the conventional one-step calcination strategy.

We further identify the change in the surface oxidation state of the catalysts depending on the presence of the Se vacancies after OER by XPS characterization as shown in Figure S22c,d, Supporting Information. The Co 2p spectrum in Figure S22c, Supporting Information, indicates the convolutional area of

Co—O peak of $Co_{0.85}Se_{0.51}\square_{0.49}$@C sample is much larger than that of $Co_{0.85}Se$@C during the OER process. And also, the O 1s spectrum in Figure S22d, Supporting Information, demonstrates the similar improvement on convolutional area of —OH group peak of $Co_{0.85}Se_{0.51}\square_{0.49}$@C compared with $Co_{0.85}Se$@C counterpart after 5000 CVs. Accordingly, it is rational that rich Se vacancies inside the sample greatly facilitate the formation of cobalt oxyhydroxides, which generally affect the activity and stability of OER. Such outstanding performance was further inherited into the transformed catalyst after the test due to the successful reservation of specific hollow nanocage structure with the presence of large amount of the carbon as followed from the decomposition of MOFs during the fabrication process.

To further understand the underlying mechanism of the activity enhancement from introducing rich selenide vacancy, we performed density functional theory (DFT) calculation. As shown in **Figure 4**, with the introduction of an Se vacancy into a $2 \times 2 \times 1$ supercell of hexagonal $Co_{0.85}Se$ crystal, the corresponding formation energy is calculated to be as low as 1.67 eV. In addition, the parameter of lattice *a* slightly decreases from 7.21 to 7.10 Å, while that of lattice *c* generally remains unchanged. Figure 4b displays the vibration properties (phonon bandstructure) of the $Co_{0.85}Se$ and $Co_{0.85}Se_{0.51}\square_{0.49}$ models, respectively. No vibrational modes at negative frequency can be observed, suggesting that both two models possess excellent structural stability. The electron properties of these two models were then further analyzed using curves of electron density of states with the results shown in Figure 4c. It can be seen that both $Co_{0.85}Se$ and $Co_{0.85}Se_{1-x}$ compounds are conductors with high density of electrons distributing on the Fermi level, mainly contributed by the hybridization of Co 3d–Se 4p. In addition, the states at Fermi level turn out to be increased with the introduction of Se vacancies, from 11.4 eV of $Co_{0.85}Se$ to 12.7 eV of $Co_{0.85}Se_{0.51}\square_{0.49}$, suggesting an improved electron conductivity originating from the unbonded Co atoms.

According to our previous TEM characterization of $Co_{0.85}Se_{0.51}\square_{0.49}$@C sample (Figure 1), the (010) surface is determined to be the major exposed surface, the four electrochemical steps for OER process on (010) surface were then investigated (Figure 4d). Another typical surface of $Co_{0.85}Se$, (001) surface was also studied for comparison with the free energy calculation results presented in Figure 4e (with the free energy calculation results concluded in Figure S23, Supporting Information). Note that on the (010) surface of $Co_{0.85}Se$, the activation free energy ($\Delta G^{\ddagger}$) from *O to *OOH (where the asterisk denotes an active site on the catalyst surface) is very high with the energy barrier of 2.04 eV. Consequently, the third step of the OER process relating with the formation of *OOH serves as the potential determining step (PDS = 0.81 eV). In the case of (001) surface, the forming of *OOH turns out to be favored with the corresponding activation free energy declines to 1.58 eV. This result indicates the last step relating with the release of $O_2$ acting as the potential determining step (PDS = 0.80 eV) during the OER process, the activation free energy of which is measured to be 2.03 eV, very close to the value on the (010) surface. After the Se vacancies are taken into consideration, the potential determining steps on both surfaces remain unchanged. However, the potential values remarkably decrease to 0.54 and 0.69 eV on (010) and (001) plane, respectively, which plays an important role in the enhancement of OER performance. Furthermore, the mapping of charge density difference on the exposed (010) surface is shown in Figure 4f. With the presence of an Se vacancy, the spare electrons from the deconstructed Co—Se bond redistribute around the exposed Co atoms, of which the valence state is found to significantly reduce from +0.248 to +0.147 (Figure 4g). Similar conclusions have been found on the (001) surface, in which case the valence state of exposed Co atoms declines from +0.252 to +0.151 with the formation of Se vacancy. The above conclusions are in well agreement with the red-shift phenomenon of Co in the XPS results (Figure 3i), implying the changes of local electronic density around Co sites in $Co_{0.85}Se_{0.51}\square_{0.49}$ crystal due to the formation of rich Se vacancies. Overall, the theoretical simulation reveals that the abundant Se vacancies considerably improve the electronic conductivity and reduce reaction barriers of $Co_{0.85}Se$, thus resulting in superior OER activity.

More importantly, our design of selenic-acid-assisted etching can be considered as a general strategy to produce rich Se vacancies in other MOFs derivatives. For example, by employing Fe-MOF and Ni-MOF as the template respectively, uniform $FeSe_{2-x}$@C nanoneedles and $NiSe_{2-x}$@C microspheres were also successfully produced by this etching strategy (Figures S24–S29, Supporting Information). Analogously, sharp EPR signal with *g*-factor = 2.003 has been detected from both $FeSe_{2-x}$@C nanoneedles and $NiSe_{2-x}$@C microspheres, demonstrating unpaired electrons trapped at Se-vacancies (**Figure 5**a,b).[33] In contrast, although no difference was detected on the phase structure and morphology of the $FeSe_2$, $NiSe_2$ counterparts prepared by the one-step calcination strategy, these counterparts delivered much lower EPR signal at the same position, corresponding to lower concentration of Se vacancies. We verified the introduction of Se vacancies in Fe, Ni-based MOF derivatives also significantly improved their catalytic properties. One can see the OER performance of vacancy-rich MOFs derivatives was much better than that of the vacancy poor counterparts: the overpotentials of 242 and 270 mV at 10 mA $cm^{-2}$ for $FeSe_{2-x}$@C nanoneedles and $NiSe_{2-x}$@C microspheres samples, respectively, much smaller than that of vacancy poor counterparts (262 and 296 mV at 10 mA $cm^{-2}$ for vacancy-poor $FeSe_2$ and $NiSe_2$ derivatives, respectively). The superior OER kinetic process of vacancy-rich samples was also confirmed by the difference on Tafel slopes as shown in Figure 5e,f. Remarkably, OER performances of our Se vacancy-rich 3d metal selenide series $M_mSe_n$ ($Co_{0.85}Se_{1-x}$, $FeSe_{2-x}$@C, $NiSe_{2-x}$@C) surpassed that of most high-performance electrocatalysts reported previously and recently, such as CoBDC-NF ($\eta$10 = 252 mV, 50 mV $dec^{-1}$),[44] Co/$\beta$-$Mo_2C$@NCNTs ($\eta$10 = 356 mV, 67 mV $dec^{-1}$),[45] NCoM-Cb-Ar ($\eta$10 = 340 mV, 76 mV $dec^{-1}$),[46] Co/CNFS(1000) ($\eta$10 = 320 mV, 79 mV $dec^{-1}$),[47] $Ag@Co(OH)_x$/CC ($\eta$10 = 250 mV, 76 mV $dec^{-1}$),[48] $Co_2Mo_3O_8$@NC ($\eta$10 = 331 mV, 87.5 mV $dec^{-1}$),[49] NiCoP ($\eta$10 = 330 mV, 96 mV $dec^{-1}$),[50] $Cs_{0.4}La_{0.6}Mn_{0.25}Co_{0.75}O_3$ ($\eta$10 = 374 mV, 101 mV $dec^{-1}$).[51]

Considered the best OER performance of $Co_{0.85}Se_{0.51}\square_{0.49}$@C sample in this series, we assembled an overall water splitting device using Pt/C as the cathode and $Co_{0.85}Se_{0.51}\square_{0.49}$@C nanocages as the anode in 1 M KOH, respectively. The polarization

 

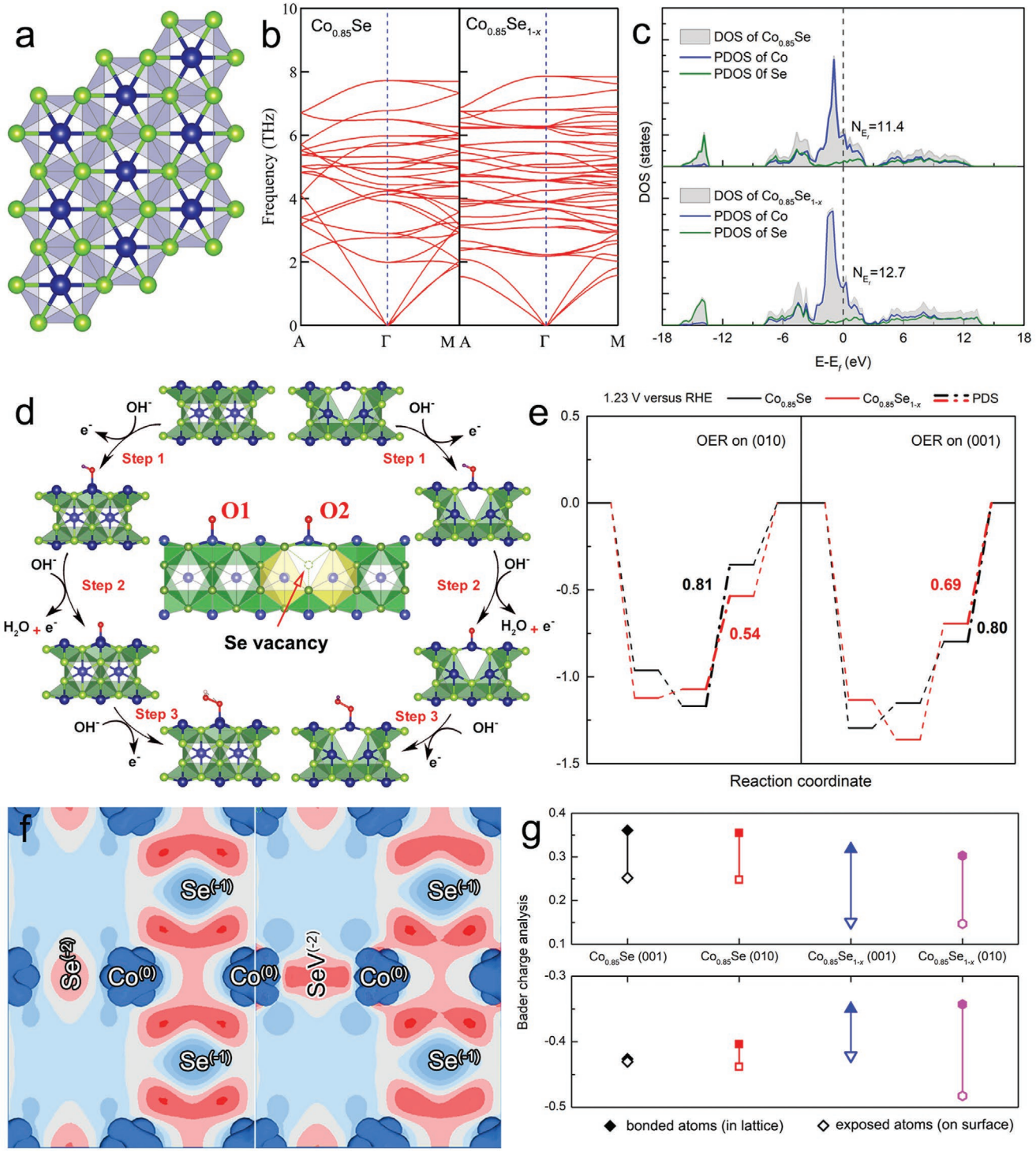


**Figure 4.** a–c) The computed structure, vibration, and electron properties of $Co_{0.85}Se$ and $Co_{0.85}Se_{0.51}\square_{0.49}$, blue and green balls represent Co and Se atoms, respectively. d,e) Simulation of the OER configurations (taking the (010) surface for example), with the corresponding free energies. f–g) Mapping of the charge density difference on the exposed surface (taking the (010) surface for example), red refers to positive area while blue refers to negative area, and the calculated valence states of Co and Se atoms via Bader charge analysis.

curve indicates that the electrolyzer required a very small cell voltage of 1.49 V to deliver a current density of 10 mA $cm^{-2}$ (Figure 5h). In addition, a solar power assisted water splitting device was used to reflect the practical application of solar water electrolysis. Figure 5i shows the optical photo of the solar power assisted water splitting device, and the voltage of the solar panel is about 1.49 V under the illumination of the sunlight. Notably, gas bubbles could be clearly observed at the surface of both

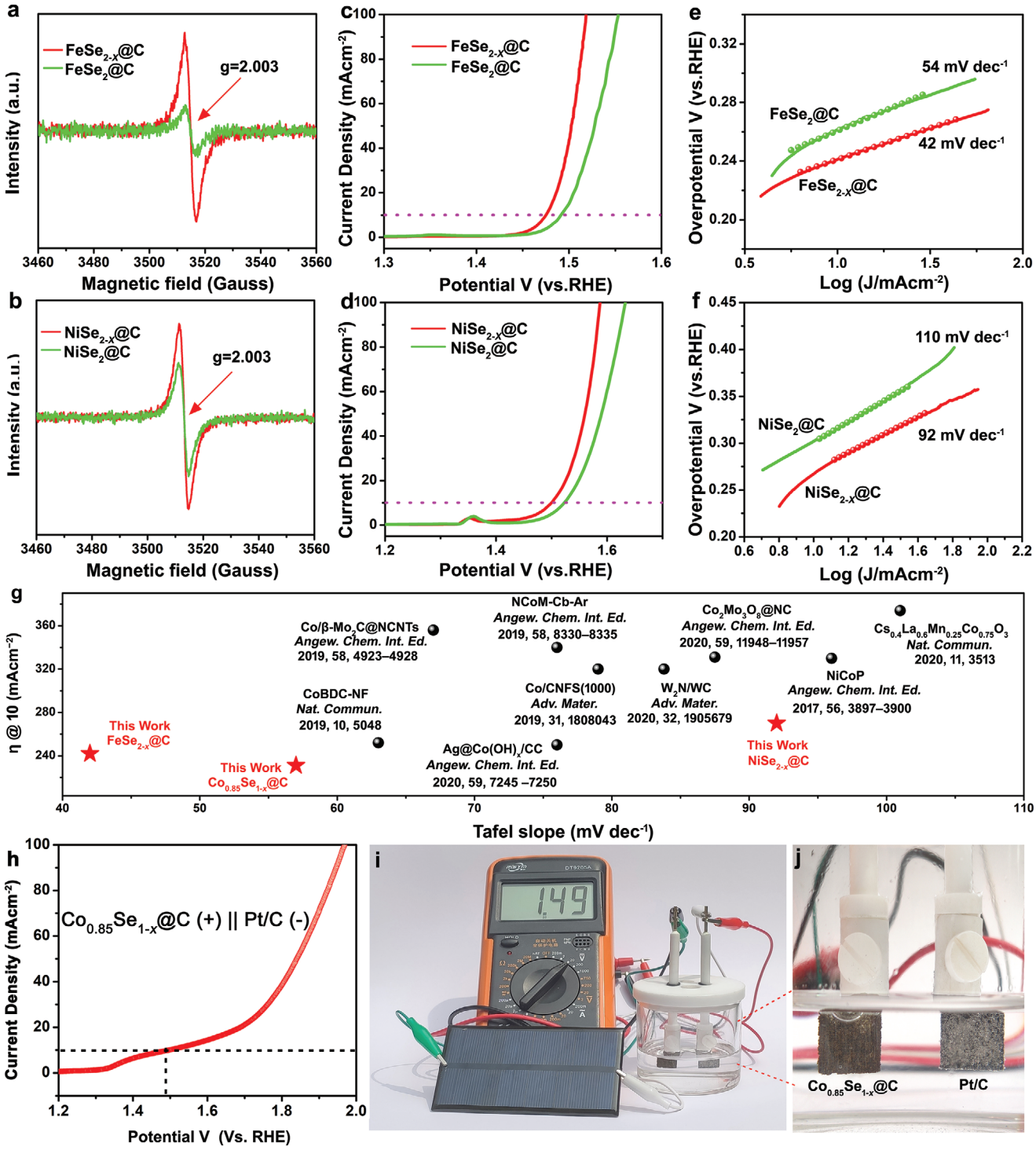


**Figure 5.** a–f) EPR spectra, LSV curves, and Tafel plots for $FeSe_{2-x}$@C, $NiSe_{2-x}$@C, $FeSe_2$@C, and $NiSe_2$@C samples, respectively (red line: Se vacancy-rich sample, green line: Se vacancy-poor sample). g) Comparison with state-of-the-art OER electrocatalysts. h–j) Polarization curves for $Co_{0.85}Se_{0.51}\square_{0.49}$@C||Pt/C device for overall water splitting in 1 M KOH (two-electrode structure) and photograph of a water-splitting device driven by a solar cell (≈1.49 V).

electrodes by powering with the solar panel (Figure 5j). This solar-assisted water splitting device is very promising for practical application on the conversion low-voltage electricity into chemical energy.

In summary, we developed a general selenic-acid-assisted etching strategy to realize a series of MOF derivatives $M_mSe_n$ ($Co_{0.85}Se_{1-x}$, $NiSe_{2-x}$, $FeSe_{2-x}$) with rich Se vacancies and uniform carbon-layer coating for high-performance OER

electrocatalysts. The abundant Se vacancies by this strategy should be originated from the weak acidity of selenic acid which cannot completely etch the MOF precursor and results in a residual ZIF-67 yolk with excess Co component in the sample. The optimal $Co_{0.85}Se_{0.51}\square_{0.49}$@C nanocages deliver an overpotential of 0.23 V at a current density of 10 mA $cm^{-2}$ and a full water-splitting electrolyzer with it as anode catalyst shows a cell voltage of 1.49 V@10 mA $cm^{-2}$ in alkaline media. DFT calculation reveals a mechanism that the introduction of abundant Se vacancies could improve conductivity and reduce reaction barriers for the formation of intermediates, thus fulfilling an important function in influencing the catalytic activity. Our study not only provides a series of metal selenides as efficient electrode for electrocatalytic oxygen evolution, but also perhaps more importantly demonstrates new opportunity to realize high-performance OER electrocatalysts by a general strategy on selenic acid etching assisted vacancy engineering.

## Experimental Section

*Preparation of the ZIF-67/Co–Se–O Yolk–Shell*: First, 100 mg of ZIF-67[52] was dispersed into 40 mL of methanol and stirred at room temperature to form mixed solution A. Then, 30 mL of aqueous solution with 50 mg of $SeO_2$ was added into 40 mL of the prepared ZIF-67 dispersion. After this, the solution was aged at room temperature for 60 min. Finally, the product was washed by ethanol three times and dried at 60 °C. The obtained product was named ZIF-1h. By modifying the aging time to 3, 5, and 10 h, ZIF-3h, ZIF-5h, and ZIF-10h were obtained, respectively.

*Preparation of $Co_{0.85}Se_{0.51}\square_{0.49}$@C Nanocages*: In brief, ZIF-67/Co–Se–O was placed in a porcelain boat. The sample was then heated up to 550 °C at a rate of 2 °C $min^{-1}$ from room temperature and held at that temperature for 2 h under Ar. After cooling down to room temperature naturally, a black powder could form, which was denoted ZIF-1h-550 (550 representing calcination at 550 °C). ZIF-1h was also calcined at 500, 600 °C under Ar atmosphere to tune the components and microstructures of the samples. The samples were named ZIF-1h-500 and ZIF-1h-600, respectively.

*Preparation of the $FeSe_{2-x}$@C Nanoneedles, $NiSe_{2-x}$@C Microsphere*: Fe/Ni MOF was synthesized under the facile solvothermal conditions previously reported.[53,54] Then $FeSe_{2-x}$@C nanoneedles were obtained by etching Fe MOF using the same method as etching ZIF-67. $NiSe_{2-x}$@C microsphere was obtained by etching Ni MOF using a method similar to etching ZIF-67 (Only reduced the amount of $SeO_2$: 12.5 mg $SeO_2$ dissolved in 15 mL $H_2O$). Finally, the precursor was calcined in Ar under 450 °C for 2 h to obtain $FeSe_{2-x}$@C nanoneedles ($NiSe_{2-x}$@C microsphere).

*Materials Characterization*: Powder X-ray diffraction (XRD) analysis was performed on a Bruker D8 Advance diffractometer with Cu-Ka radiation $\lambda = 0.15406$ nm. Raman spectra were collected on a Renishaw in via spectrometer with an excitation laser wavelength of 457.9 nm. X-ray photoelectron spectra (XPS, PHI 5000C EACA system XPS using an Mg K$\alpha$) were performed to obtain the elemental composition and chemical state of the materials. The morphologies of as-obtained products were observed by scanning electron microscopy (SEM) (Hitachi S-4800 electron microscopy). Transmission electron microscopy (TEM) and high-resolution TEM (HRTEM) were performed on a JEM-2100F Field Emission Electron microscope, respectively. TGA measurements were carried out using an SDT Q600 instrument in a temperature range of room temperature to 800 °C with a heating rate of 2 °C $min^{-1}$ under a stream of air. The ICP test was performed using a PerkinElemer Optima 8000 analyzer. Specific surface area was examined by the Brunauer–Emmett–Teller (BET) method using $N_2$ adsorption–desorption isotherms on an autosorb iQ at liquid nitrogen temperature (77 K). EPR spectra were recorded from a Bruker A 300 at 77 K.

*Electrochemical Measurement*: All electrochemical measurements were carried out on the electrochemical workstation (CHI 760 E) in 1 M KOH (pH = 13.8). The glassy carbon electrode (GCE, radius of 2 mm for OER), a graphite rod, and Hg/HgO electrode were used as the working electrode, the counter electrode, and the reference electrode, respectively. Typically, 5 mg of catalyst was dispersed in 40 µL Nafion and 1 mL water and ethanol solution (The volume ratio of water and ethanol was 1:1).[55] Then a total of 20 µL of the catalysis slurry was dropped onto the surface of the bare GCE. The loading of the catalyst was 0.796 mg $cm^{-2}$. Before the electrochemical measurements, the electrolyte was purged with $N_2$ for 1 h to remove the dissolved gases completely. All the potentials were quoted with respect to the reversible hydrogen electrode (RHE) through $E_{RHE} = E_{HgO/Hg} + 0.059 \times pH + 0.095$ V. Cyclic voltammetry (CV) was conducted at a scan rate of 100 mV $s^{-1}$ to activate the catalysts. The linear sweep voltammograms (LSV) curves were collected at a sweep rate of 2 $mVs^{-1}$ with 90% IR compensation. The resulting polarization curves were *iR*-compensated according to the equation: $E_c = E_m - iR_s$ ($E_c$ is the corrected potential, $E_m$ is the measured potential experimentally, $R_s$ is the resistance of the ohmic resistance arising from the electrolyte/contact resistance of the setup and measured by electrochemical impedance spectroscopy). Long-term stability tests were carried out by using chronoamperometry measurement method. The electrochemical impedance spectroscopy measurements were tested by applying an AC voltage with 5 mV amplitude in a frequencies changing from 100 kHz to 0.1 Hz at overpotential of 345 mV. Cyclic voltammetry was conducted to probe the double-layer capacitor ($C_{dl}$) to calculate the electrochemically active surface area (ECSA). The above tests were all performed at room temperature (25 °C). In overall water splitting tests, the $Co_{0.85}Se_{0.51}\square_{0.49}$@C and Pt/C were used as anode and cathode respectively in a two-electrode reactor for overall water splitting. The loadings of $Co_{0.85}Se_{0.51}\square_{0.49}$@C and Pt/C on the Ni foam were about 2.5 mg $cm^{-2}$.

*Electron Paramagnetic Resonance Measurement*: EPR spectra were obtained by a Bruker A300 spectrometer working in the X-band and calibrated with a DPPH standard ($g = 2.0036$). 10 mg the solid-state catalysts were carefully collected by a razor blade and then they were transferred to an EPR tube under Ar (99.999%) atmosphere. The EPR tube was immediately frozen and stored at 77 K using liquid nitrogen before measurement. The following parameters were used: microwave frequency: 9.64 GHz, modulation amplitude: 10 G, modulation frequency: 100 kHz, microwave power: 0.94 mW, and temperature: 77 K. Then scans were added for obtaining each spectrum.

*Density Functional Theory Simulation*: The simulation in this work was performed in the framework of DFT as implemented in the Vienna Ab initio Simulation Package (VASP). The projector augmented wave method (PAW) and the generalized gradient approximation constructed by Perdew–Burke–Ernzerhof (GGA-PBE) for the exchange-correlation energy function were used. In addition, the Hubbard-like +U approach was applied to mitigate the delocalization error of GGA functional for treating transition metal atoms: $U_{eff} = U - J = 5.0$ eV for Co atoms. The cutoff energy was set to be 500 eV in this work, together with a Γ-centered *k*-grid scheme with a total number of 50. Finally, the convergence criterion for the electronic self-consistent iteration was set to be $10^{-4}$ eV, and the atomic positions were fully relaxed until the force on each atom was less than 0.02 eV $Å^{-1}$.

## Supporting Information

Supporting Information is available from the Wiley Online Library or from the author.

## Acknowledgements

L.Z. and C.L. contributed equally to this work. This work was financially supported by the National Natural Science Foundation of China (Nos. 51872051, 51731004, 51701042), the Science and Technology Committee

of Shanghai Municipality (18520723100), the Researching Program of State Grid Corporation of China (GYW17201800011).

## Conflict of Interest

The authors declare no conflict of interest.

## Data Availability Statement

Research data are not shared.

## Keywords

electrocatalysts, metal selenides, oxygen evolution reaction, selenic-acid-assisted etching, selenium vacancies

Received: November 3, 2020
Revised: December 23, 2020
Published online: March 3, 2021

[1] N. Zhang, X. B. Feng, D. W. Rao, X. Deng, L. J. Cai, B. C. Qiu, R. Long, Y. J. Xiong, Y. Lu, Y. Chai, *Nat. Commun.* **2020**, *11*, 4066.
[2] M. J. Craig, G. Coulter, E. Dolan, J. S. L. López, E. M. Torres, W. G. Schmitt, M. G. Melchor, *Nat. Commun.* **2019**, *10*, 4993.
[3] J. Wang, F. Xu, H. Y. Jin, Y. Q. Chen, Y. Wang, *Adv. Mater.* **2017**, *29*, 1605838.
[4] L. Li, B. Wang, G. W. Zhang, G. Yang, T. Yang, S. Yang, S. C. Yang, *Adv. Energy Mater.* **2020**, *10*, 2001600.
[5] H. J. Yan, Y. Xie, A. P. Wu, Z. C. Cai, L. Wang, C. G. Tian, X. M. Zhang, H. G. Fu, *Adv. Mater.* **2019**, *31*, 1901174.
[6] J. Zhang, Q. Y. Zhang, X. L. Feng, *Adv. Mater.* **2019**, *31*, 1808167.
[7] Y. M. Zhu, Z. Y. He, Y. M. Choi, H. J. Chen, X. B. Li, B. Zhao, Y. Yu, H. Zhang, K. A. Stoerzinger, Z. X. Feng, Y. Chen, M. L. Liu, *Nat. Commun.* **2020**, *11*, 4299.
[8] Y. Yang, H. Q. Yao, Z. H. Yu, S. M. Islam, H. Y. He, M. W. Yuan, Y. H. Yue, K. Xu, W. C. Hao, G. B. Sun, H. F. Li, S. L. Ma, P. Zapol, M. G. Kanatzidis, *J. Am. Chem. Soc.* **2019**, *141*, 10417 .
[9] A. P. Wu, Y. Xie, H. Ma, C. G. Tian, Y. Gu, H. J. Yan, X. M. Zhang, G. Y. Yang, H. G. Fu, *Nano Energy* **2018**, *44*, 353.
[10] J. Saha, S. Verma, R. Ball, C. Subramaniam, R. Murugavel, *Small* **2020**, *16*, 1903334.
[11] F. Song, X. L. Hu, *Nat. Commun.* **2014**, *5*, 4477.
[12] G. R. Cai, W. Zhang, L. Jiao, S. H. Yu, H. L. Jiang, *Chem* **2017**, *2*, 791.
[13] J. Liu, S. J. Hou, W. J. Li, A. S. Bandarenka, R. A. Fischer, *Chem. Asian J.* **2019**, *14*, 3474.
[14] M. Hu, S. Furukawa, R. Ohtani, H. Sukegawa, Y. Nemoto, J. Reboul, S. Kitagawa, Y. Yamauchi, *Angew. Chem., Int. Ed.* **2012**, *51*, 984.
[15] S. L. Zhang, B. Y. Guan, X. F. Lu, S. B. Xi, Y. H. Du, X. W. Lou, *Adv. Mater.* **2020**, *32*, 2002235.
[16] J. G. Li, H. C. Sun, L. Lv, Z. S. Li, X. Ao, C. H. Xu, Y. Li, C. D. Wang, *ACS Appl. Mater. Interfaces* **2019**, *11*, 8106.
[17] X. Qian, W. M. Wu, Y. Niu, J. H. Yang, C. Xu, K. Y. Wong, *ACS Appl. Mater. Interfaces* **2019**, *11*, 43278.
[18] X. Wang, F. Li, W. Z. Li, W. B. Gao, Y. Tang, R. Li, *J. Mater. Chem. A* **2017**, *5*, 17982.
[19] Y. M. Zhu, X. Liu, S. G. Jin, H. J. Chen, W. Y. Lee, M. L. Liu, Y. Chen, *J. Mater. Chem. A* **2019**, *7*, 5875.
[20] D. X. Yang, Q. G. Zhu, X. F. Sun, C. J. Chen, W. W. Guo, G. Y. Yang, B. X. Han, *Angew. Chem.* **2020**, *132*, 2374.
[21] Z. Q. Hou, P. Hei, C. Z. Shu, R. X. Zheng, T. S. Yang, Q. Zhang, J. P. Long, *ACS Sustainable Chem. Eng.* **2020**, *8*, 6667.
[22] Y. X. Zhang, C. Zhang, Y. M. Guo, D. L. Liu, Y. F. Yu, B. Zhang, *J. Mater. Chem. A* **2019**, *7*, 2536.
[23] M. Q. Yang, J. Wang, H. Wu, G. W. Ho, *Small* **2018**, *14*, 1703323.
[24] D. S. Kong, H. T. Wang, Z. Y. Lu, Y. Cui, *J. Am. Chem. Soc.* **2014**, *136*, 4897.
[25] Y. W. Liu, H. Cheng, M. J. Lyu, S. J. Fan, Q. H. Liu, W. S. Zhang, *J. Am. Chem. Soc.* **2014**, *136*, 15670.
[26] Y. C. Jiang, Y. Song, Z. C. Pan, Y. Meng, L. Jiang, Z. Y. Wu, P. Y. Yang, Q. F. Gu, D. L. Sun, L. F. Hu, *ACS Nano* **2018**, *12*, 5011.
[27] Y. C. Jiang, Z. Y. Wu, L. Jiang, Z. C. Pan, P. Y. Yang, W. C. Tian, L. F. Hu, *Nanoscale* **2018**, *10*, 12003.
[28] Z. X. Cai, Z. L. Wang, J. H. Kim, Y. S. Yamauchi, *Adv. Mater.* **2019**, *31*, 1804903.
[29] X. X. Wang, Z. L. Na, D. M. Yin, C. L. Wang, Y. M. Wu, G. Huang, L. M. Wang, *ACS Nano* **2018**, *12*, 12238.
[30] T. Wang, C. Yang, Y. J. Liu, M. Yang, X. F. Li, Y. He, H. M. Li, H. B. Chen, Z. Q. Lin, *Nano Lett.* **2020**, *20*, 5639.
[31] H. B. Wu, B. Y. Xia, L. Yu, X. Y. Yu, X. W. Lou, *Nat. Commun.* **2015**, *6*, 1.
[32] C. F. Chen, A. P. Wu, H. J. Yan, Y. L. Xiao, C. G. Tian, H. G. Fu, *Chem. Sci.* **2018**, *9*, 4746.
[33] H. He, D. Huang, Q. M. Gan, J. N. Hao, S. L. Liu, Z. B. Wu, W. K. Pang, B. Johannessen, Y. G. Tang, J. L. Luo, H. Y. Wang, Z. P. Guo, *ACS Nano* **2019**, *13*, 11843.
[34] G. Yilmaz, K. M. Yam, C. Zhang, H. J. Fan, G. W. Ho, *Adv. Mater.* **2017**, *29*, 1606814.
[35] M. Jana, P. Sivakumara, M. Kota, M. G. Jung, H. S. Park, *J. Power Sources* **2019**, *422*, 9.
[36] Z. J. Chen, Q. Kang, G. X. Cao, N. Xu, H. B. Dai, P. Wang, *Int. J. Hydrogen Energy* **2018**, *43*, 6076.
[37] X. Xu, F. Song, X. L. Hu, *Nat. Commun.* **2016**, *7*, 12324.
[38] T. Meng, J. W. Qin, S. G. Wang, D. Zhao, B. G. Mao, M. H. Cao, *J. Mater. Chem. A* **2017**, *5*, 7001.
[39] Y. X. Huang, Z. H. Wang, Y. Jiang, S. J. Li, Z. H. Li, H. Q. Zhang, F. Wu, M. Xie, L. Li, R. J. Chen, *Nano Energy* **2018**, *53*, 524.
[40] Y. Sun, J. Meng, H. X. Ju, J. Zhu, Q. X. Li, Q. Yang, *J. Mater. Chem. A* **2018**, *6*, 22526.
[41] Y. Sun, X. W. Zhang, B. G. Mao, M. H. Cao, *Chem. Commun.* **2016**, *52*, 14266.
[42] J. H. Lin, H. H. Wang, J. Cao, F. He, J. Feng, J. L. Qi, *J. Colloid Interface Sci.* **2020**, *571*, 260.
[43] T. T. Zheng, C. Y. Shang, Z. H. He, X. Y. Wang, C. Cao, H. L. Li, R. Si, B. C. Pan, S. M. Zhou, J. Zeng, *Angew. Chem., Int. Ed.* **2019**, *58*, 14764.
[44] Z. Q. Xue, K. Liu, Q. L. Liu, Y. L. Li, M. R. Li, C. Y. Su, N. Ogiwara, H. Kobayashi, H. Kitagawa, M. Liu, G. Q. Li, *Nat. Commun.* **2019**, *10*, 5048.
[45] T. O. yang, Y. Q. Ye, C. Y. Wu, K. Xiao, Z. Q. Liu, *Angew. Chem., Int. Ed.* **2019**, *58*, 4923.
[46] R. Gond, D. K. Singh, M. Eswaramoorthy, P. Barpanda, *Angew. Chem., Int. Ed.* **2019**, *58*, 8330.
[47] Z. K. Yang, C. M. Zhao, Y. T. Qu, H. Zhou, F. Y. Zhou, J. Wang, Y. Wu, Y. D. Li, *Adv. Mater.* **2019**, *31*, 1808043.
[48] Z. Zhang, X. P. Li, C. Zhong, N. Q. Zhao, Y. Deng, X. P. Han, W. B. Hu, *Angew. Chem., Int. Ed.* **2020**, *59*, 7245.
[49] T. Ouyang, X. T. Wang, X. Q. Mai, A. N. Chen, Z. Y. Tang, Z. Q. Liu, *Angew. Chem., Int. Ed.* **2020**, *59*, 11948.
[50] P. L. He, X. Y. Yu, X. W. Lou, *Angew. Chem., Int. Ed.* **2017**, *56*, 3897.
[51] B. C. Weng, Z. L. Song, R. L. Zhu, Q. Y. Yan, Q. Sun, C. G. Grice1, Y. F. Yan, W. J. Yin, *Nat. Commun.* **2020**, *11*, 3513.
[52] K. Y. A. Lin, H. A. Chang, J. Taiwan, *J. Taiwan Inst. Chem. Eng.* **2015**, *53*, 40.
[53] X. J. Xu, J. Liu, J. W. Liu, L. Z. Ouyang, R. Z. Hu, H. Wang, L. C. Yang, M. Zhu, *Adv. Funct. Mater.* **2018**, *28*, 1707573.
[54] M. K. Wu, C. Chen, J. J. Zhou, F. Y. Yi, K. Tao, L. Han, *J. Alloys Compd.* **2018**, *734*, 1.
[55] J. Y. Qin, Z. W. Liu, D. Y. Wu, J. Yang, *Appl. Catal. B: Environ.* **2020**, *278*, 119300.